# SuperCAM CO(3-2) APEX survey at a 6 pc resolution in the Small Magellanic Clouds

(article starts on next page)

# SuperCAM CO(3–2) APEX survey at a 6 pc resolution in the Small Magellanic Clouds[⋆]

H. P. Saldaño[1,2] , M. Rubio[3] , A. D. Bolatto[4], K. Sandstrom[5], B. J. Swift[6], C. Verdugo[7], K. Jameson[8], C. K. Walker[6], C. Kulesa[6] , J. Spilker[9], P. Bergman[10], and G. A. Salazar[1,2]

[1] Instituto de Investigaciones en Energía no Convencional, Universidad Nacional de Salta, C.P. 4400, Salta, Argentina
e-mail: hpablohugo@gmail.com
[2] Consejo Nacional de Investigaciones Científicas y Técnicas (CONICET), Godoy Cruz 2290, CABA, CPC 1425FQB, Argentina
[3] Departamento de Astronomía, Universidad de Chile, Casilla 36-D, Santiago, Chile
[4] Department of Astronomy and Joint Space-Science Institute, University of Maryland, College Park, MD 20742, USA
[5] Center for Astrophysics & Space Sciences, Department of Physics, University of California, San Diego, 9500 Gilman Drive, San Diego, CA 92093, USA
[6] Department of Astronomy and Steward Observatory, University of Arizona, Tucson, AZ 85719, USA
[7] Joint ALMA Observatory (JAO), Alonso de Córdova 3107, Vitacura, Santiago de Chile
[8] Owens Valley Radio Observatory, California Institute of Technology, Big Pine, CA 93513, USA
[9] Department of Physics and Astronomy and George P. and Cynthia Woods Mitchell Institute for Fundamental Physics and Astronomy, Texas A&M University, College Station, TX, USA
[10] Onsala Space Observatory, Department of Space, Earth and Environment, Chalmers University of Technology, 439 92 Onsala, Sweden

## ABSTRACT

*Context.* The Small Magellanic Cloud (SMC) is an ideal laboratory for studying the properties of star-forming regions thanks to its low metallicity, which has an impact on the molecular gas abundance. However, a small number of molecular gas surveys of the entire galaxy have been carried out in the last few years, limiting the measurements of interstellar medium (ISM) properties in a homogeneous manner.
*Aims.* We present the CO(3–2) APEX survey at a 6 pc resolution of the bar of the SMC, observed with the SuperCAM receiver attached to the APEX telescope. This high-resolution survey has allowed us to study certain properties of the ISM and to identify CO clouds in the innermost parts of the $H_2$ envelopes.
*Methods.* We adopted the CO analysis in the SMC bar comparing the CO(3–2) survey with that of the CO(2–1) of a similar resolution. We studied the CO(3–2)-to-CO(2–1) ratio ($R_{32}$), which is very sensitive to the environment properties (e.g., star-forming regions). We analyzed the correlation of this ratio with observational quantities that trace the star formation such as the local CO emission, the Spitzer color [70/160], and the total IR surface brightness measured from the Spitzer and Herschel bands. For the identification of the CO(3–2) clouds, we used the CPROPS algorithm, which allowed us to measure the physical properties of the clouds. We analyzed the scaling relationships of such physical properties.
*Results.* We obtained $R_{32} = 0.65 \pm 0.02$ for the SW bar and a slightly higher ratio, $R_{32} = 0.7 \pm 0.1$, for N66 in the SMC. We found that $R_{32}$ varies from region to region, depending on the star formation activity. In regions dominated by HII and photo-dissociated regions (e.g., N22, N66) $R_{32}$ tends to be higher than the median values. Meanwhile, lower values were found toward quiescent clouds. We also found that $R_{32}$ is correlated with the IR color [70/160] and the total IR surface brightness. This finding indicates that $R_{32}$ increases with environmental properties, such as the dust temperature, total gas density, and radiation field. We identified 225 molecular clouds with sizes of $R > 1.5$ pc and signal-to-noise ratios (S/N) of >3, of which only 17 are well resolved CO(3–2) clouds with $S/N \gtrsim 5$. These 17 clouds follow consistent scaling relationships to the inner Milky Way clouds but with some departures. For instance, CO(3–2) tends to be less turbulent and less luminous than the inner Milky Way clouds of similar sizes. Finally, we estimated a median virial-based CO(3–2)-to-$H_2$ conversion factor of $12.6^{+10}_{-7}$ $M_\odot$ (K km s$^{-1}$ pc$^2$)$^{-1}$ for the total sample.

**Key words.** ISM: abundances – ISM: clouds – ISM: molecules – galaxies: dwarf – galaxies: individual: SMC – submillimeter: ISM

## 1. Introduction

The Small Magellanic Cloud (SMC) is the nearest low-metallicity galaxy to the Milky Way (∼60 kpc, Hilditch et al. 2005), with a low metal abundance ($Z \approx 0.2$ $Z_\odot$, Russell & Dopita 1992) and a high gas-to-dust ratio (GDR

∼2000, Roman-Duval et al. 2017). It presents a challenge in the study of the molecular component of the interstellar medium (ISM) and its association with star-forming regions. The low dust content prevents protection from the high ultraviolet (UV) radiation field, allowing for a strong dissociation of most of the molecular gas at low $A_V$, specifically carbon monoxide (CO), a common tracer of $H_2$ gas.

Theoretical models (Wolfire et al. 2010; Seifried et al. 2020) have shown that due to the strong $H_2$ self-shielding, the $H_2$ molecule starts to form in low-hydrogen-nuclei density

---

($n_H$ = 10–$10^3$ cm$^{-3}$) regions where $A_V$ takes values from 0.2 to 1.5 mag. These molecular $H_2$ regions, also containing neutral (C) and ionized carbon (C$^+$) but without CO gas, are frequently embedded within strong photodissociation regions (PDRs) that are well traced by the [CII] emission at 158 μm (see also Requena-Torres et al. 2016; Pineda et al. 2017; Jameson et al. 2018). These molecular envelopes where CO is not present are known as "dark molecular gas." At higher densities ($n_H >$ 300 cm$^{-3}$), where $A_V \gtrsim 1.5$ and the temperatures are below ∼50 K, the carbon is present as CO and becomes the most abundant molecular component after the $H_2$ molecule ("bright CO gas"). Generally, in normal conditions such as those present in the inner Milky Way, the total molecular gas traced by CO makes a 60% to 80% contribution (Wolfire et al. 2010). However, at very low metallicities, such as that of the SMC, the molecular and atomic carbon distributions change considerably – to the degree that the CO filling fraction can be several orders of magnitude lower than those of their Galactic counterparts (Bolatto et al. 2013; Kalberla et al. 2020). In the SMC, the CO gas only would trace less than 30% (Pineda et al. 2017; Jameson et al. 2018) of the total $H_2$ gas in the innermost part of the molecular clouds (see also Oliveira et al. 2011). The bright CO gas fraction may also be reduced in magnetized molecular clouds (Seifried et al. 2020). These characteristics make the analysis of the molecular gas in the SMC difficult, limiting studies to small CO structures embedded in larger $H_2$ clouds.

Despite the fact that CO becomes a less efficient indicator of the total $H_2$ gas in low metallicity galaxies, CO observations at different transitions in the SMC (Bolatto et al. 2008; Rubio et al. 2000; Muller et al. 2014; Jameson et al. 2018; Oliveira et al. 2019; Saldaño et al. 2023) have enabled analyses of the dynamical state and observational properties (e.g., the integrated CO line ratio) of cold molecular clouds, where star formation is expected to take place. Multi-transitional models (Peñaloza et al. 2018) and observations of the CO emission in different galaxies (den Brok et al. 2021; Leroy et al. 2022) have shown that CO line ratios of various transitions are very sensitive to the physical conditions of the environment. These include the dust temperature, column density, interstellar radiation field (ISRF), cosmic ray, and star formation rate (SFR).

The first rotational transitions of CO ($J$ = 1–0 and $J$ = 2–1) trace the cold bright CO gas of low density thanks to its low excitation energies ($E_u/k$ = 5.5–16.6 K) and lower critical densities ($10^3 \lesssim n_{crit} \lesssim 10^4$ cm$^{-3}$). Higher $J$ transitions, such as CO($J$ = 3–2), are required to study warmer and denser regions of molecular clouds, as this transition has an excitation energy of $E_u/k$ = 33 K and a critical density of $n_{crit} \sim 7 \times 10^4$ cm$^{-3}$. Therefore, combining higher $J$ transitions with lower $J$ transitions allows for better constraints to be placed on the temperatures and densities within the molecular clouds.

In the SMC, Bolatto et al. (2003) found a CO(2−1)/CO(1−0) integrated line brightness ratio $\gtrsim 2$ (at 43″ resolution) in the N83/N84 molecular cloud. The high ratio is associated with an expanding molecular shell which coincides with the NGC 456 stellar association and a supernova remnant. Nikolić et al. (2007), performed a multi-transitional study of CO in six different regions of the SMC, which included quiescent clouds with no signs of star formation activity and other clouds with evident star formation activity. In the first case, low CO(2−1)/CO(1−0) and CO(3−2)/CO(1−0) ratios (at 45″ resolution) with values of ≲0.5 were found in a warm (50 K) and relatively dense gas ($n_{H_2}$ = 700 cm$^{-3}$) but quiescent molecular cloud SMCB1#1. However, higher CO(2−1)/CO(1−0) and CO(3−2)/CO(1−0)

ratios (≳1) were found in other regions associated with prominent star formation, such as N12, N27, N66, and N83. In these active regions, the observed line ratios were reproduced by a two-component model comprised of a cold dense component ($T_k$ = 10–150 K, $n_{H_2}$ = $10^4$–$10^5$ cm$^{-3}$) and a hot tenuous component ($T_k$ = 100–300 K, $n_{H_2}$ = $10^2$–$10^3$ cm$^{-3}$).

In terms of the Magellanic Bridge (MB), Muller et al. (2014) carried out a study of the CO(3−2)/CO(1−0) in several clouds at 22″ resolution. A much higher CO(3−2)/CO(1−0) ratio of ∼2.5 was found towards the cloud MB-B, which is associated with recent or current star formation. However, this high ratio is not seen in other sites of the Magellanic Bridge, such as the clouds MB-A and MB-C, which show a CO(3−2)/CO(1−0) ratio of ≲1. These clouds may be remnants of a past period of star formation.

Toward the Large Magellanic Clouds (LMC), high CO(3−2)/CO(1−0) ratios between ∼1–2 were found in warm (60–80 K) and dense ($n_{H_2} > 10^3$ cm$^{-3}$) clouds, which are correlated with the 24 μm and Hα peak emission (Minamidani et al. 2008; Mizuno et al. 2010), while lower ratios were found in cooler and lower dense clouds poorly associated with star-forming indicators (see also Celis Peña et al. 2019). In the starburst-like galaxy NGC 1140, Hunt et al. (2017) found that high $R_{31} \sim 2$ is an indication of high $H_2$ density (∼$10^6$ cm$^{-3}$) in cool clouds (≲20 K) and also a sign of somewhat excited, optically thin gas.

In this paper, we present a CO(3–2) survey of the main body of the SMC (SMC bar) performed with SuperCAM attached to the APEX telescope at 6 pc resolution. In combination with the CO(2–1) survey of the SMC (Saldaño et al. 2023), we have determined the CO(3–2)-to-CO(2–1) ratio of the SMC and studied this ratio for clouds located in different environments within the galaxy. In addition, we have derived and analyzed the physical properties of the CO(3–1) clouds and studied their scaling relations. Our results will impact the study of external galaxies where CO(3–2) emission is being used to determine the mass and properties of the molecular gas. In the following section, we detail the reduction of the SuperCAM data and we show the complementary data used for the analysis. In Sect. 3, we show the methodology used to estimate the CO(3–2)-to-CO(2–1) ratio in different parts of the SMC. In Sect. 4, we explain the cloud identification by the CPROPS algorithm. In Sect. 5, we give the main results, while in Sect. 6, we present a discussion of the main results. Finally, In Sect. 7, we present the conclusion and final remarks.

## 2. Data and reduction

### 2.1. CO(3–2) observations

The SMC survey was performed using the SuperCAM multi-pixel focal plane array of superconducting mixers attached to the 12 m Atacama Pathfinder EXperiment (APEX[1]) (Güsten et al. 2006) telescope, located in Llano de Chajnantor, near San Pedro de Atacama, Northern Chile. The galaxy was mapped in the CO(3−2) line during the period the visiting instrument SuperCAM was deployed. The observations were done on two dates, 2014 December 08, and 2015 May 16, 2015 (PI. M. Rubio, Project C-095.F-9707B, C-094.F-9306A, PI. A. Bolatto O-094.F-9306A).

**Table 1.** Characteristics of the SuperCAM CO(3–2) observations in the SMC.

| SMC | RA (hh:mm:ss.s) | Dec (dd:mm:ss.s) | FoV (°×°) | HPBW (arcsec) | $\Delta V^{(a)}$ (km s$^{-1}$) | $T_{\rm rms}^{(b)}$ (K) |
|---|---|---|---|---|---|---|
| SWBAR | 00:48:18.8 | −73:18:05.5 | $1.1 \times 1.2$ | 20 | 0.4 | 1.0 |
| MID | 00:54:48.5 | −72:28:27.9 | $1.1 \times 1.2$ | 20 | 0.4 | 0.8 |
| N | 01:03:43.0 | −72:12:36.5 | $1.1 \times 0.8$ | 20 | 0.4 | 0.9 |

**Notes.** $^{(a)}$The original cubes ($\Delta V = 0.23$ km s$^{-1}$) were re-sampled to a spectral resolution of 0.4 km s$^{-1}$ to increase the S/N ratio. $^{(b)}$The median $T_{\rm rms}$ is calculated using a 0.4 km s$^{-1}$ spectral resolution.



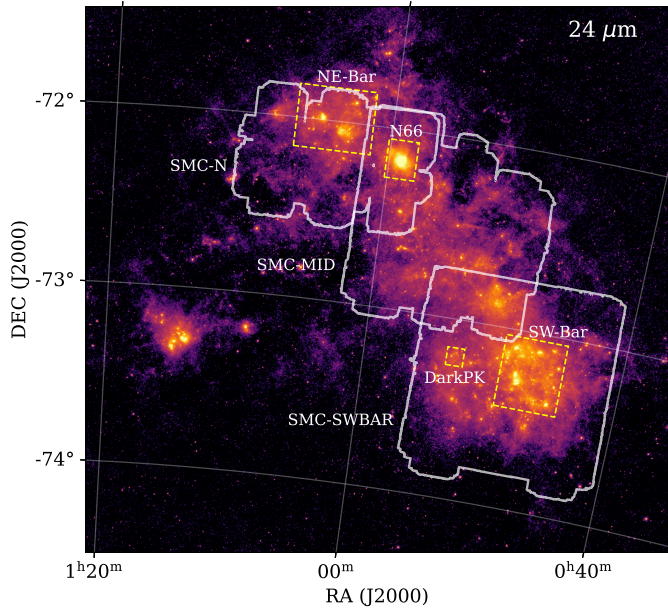**Fig. 1.** SuperCAM observations of the SMC delineated by white contours. These contours are superimposed on the 24 μm SAGE-SMC image (Gordon et al. 2011). The yellow boxes show the CO(2–1) APEX maps (Saldaño et al. 2023).

SuperCAM consists of a 64-pixel 345 GHz heterodyne imaging spectrometer designed to operate in the astrophysically important 870 μm atmospheric window (Walker et al. 2005). This camera was built by the Steward Observatory Radio Astronomy Laboratory (SORAL[2]), a project belonging to the University of Arizona and is by far the largest such array used to perform very large surveys of the sky. For instance, it was used to map a 2.7 square degree area of the Orion molecular cloud complex (Stanke et al. 2022). For more technical details of the array receiver, we refer to Groppi et al. (2010) and Kloosterman et al. (2012).

The SMC was mapped in multiple overlapping regions of size ~20′ × 10′ using the on-the-fly (OTF) mode. These maps were later combined to improve the signal-to-noise ratio (S/N) of different regions of the galaxy. This process generated three large maps, SMC-SWBAR, SMC-MID, and SMC-N, that cover most of the SMC-BAR as is shown in Fig. 1. In the figure, the white contours show the observed SuperCAM area superimposed on the 24 μm emission image. The figure also shows the areas of CO(2–1) mapping (Saldaño et al. 2023). The reduction of the OTF maps, as well as the combination of all of them, were made using an automatic procedure following a set

<hr>

[2] http://soral.as.arizona.edu/Supercam/Welcome.html

of GILDAS/CLASS and Python algorithms developed by the SORAL team, which include the baseline fitting to each spectrum in the cubes using a linear polynomial fit. As a reference for the baseline fitting, we used the NANTEN CO(1–0) data cube (Mizuno et al. 2001; Mizuno 2009).

The antenna temperature, $T_A$, was transformed to brightness temperature of the main beam ($T_{\rm mb} = T_A/\eta_{\rm mb}$) using the telescope beam efficiency $\eta_{\rm mb} = 0.38$. The final reduction produced CO(3–2) cubes with a spatial resolution of HPBW = 20″ (~6 pc at the SMC distance) and a spectral resolution of 0.233 km s$^{-1}$. To further increase the S/N ratio of the cubes, we re-sampled the velocity axis to a spectral resolution of 0.4 km s$^{-1}$. The median intensity *rms* of the mapped region is ~1 K. The final SMC-SWBAR and SMC-MID cubes have sizes of ~1°.1 × 1°.2, while the SMC-N cube has a size of ~1°.1 × 0°.8. These observational parameters, including the equatorial coordinates and the field-of-view (FoV in Col. 4) for each map, are indicated in Table 1.

To obtain the final SMC bar CO(3–2) cube, we performed a mosaicing with the SMC-SWBAR, SMC-MID and SMC-N cubes. We show the integrated CO(3–2) emission of the SMC bar in Fig. 2. The integration was performed within the velocity range of the clouds with $S/N > 3$. We included an artificial homogeneous background noise in the map to enhance the appearance of the detected clouds. In Appendix A, we show the rms map of the CO(3–2) emission.

### 2.2. Complementary data

We used the APEX SMC CO(2–1) survey reported by Saldaño et al. (2023). The APEX CO(2–1) survey has a spatial and spectral resolution of 30″ (~9 pc at the SMC distance) and $\Delta V = 0.25$ km s$^{-1}$, respectively, and covers a subset of regions in the SMC, namely SW bar, NE bar, N66, and DarkPK, which are shown in Fig. 1 by yellow boxes. The CO(2–1) *rms* intensity of the regions vary between ~0.1–0.3 K.

We also used the Infrared Array Camera (IRAC) 8 μm image and the Multiband Imaging Photometer (MIPS) 24, 70, and 160 μm images from the Spitzer survey titled Surveying the Agents of Galaxy Evolution (SAGE; Gordon et al. 2011). We also included in the analysis the HERITAGE Herschel data in the three bands 100 μm, 160 μm, and 250 μm from Gordon et al. (2014) and the Hα image from the Magellanic Cloud Emission-Line Survey (MCELS, Winkler et al. 2015).

## 3. CO(3–2)-to-CO(2–1) ratio

We are interested in quantifying the $R_{32} = [\text{CO}(3–2)/\text{CO}(2–1)]$ ratio in the SMC. This ratio can be determined only towards the common areas in both transitions as the CO(2–1) maps do not
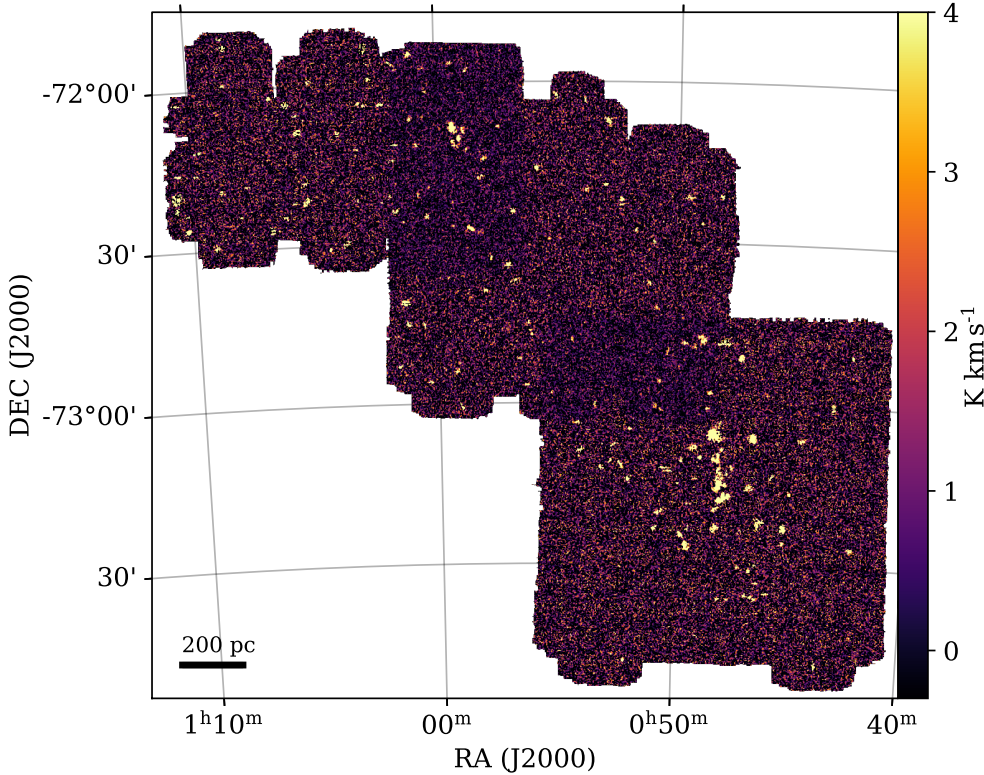
**Fig. 2.** CO(3–2) integrated map of the SMC bar observed by SuperCAM. The integration was done within the velocity range of clouds with high S/N ratios (>3). We included an artificial homogeneous background noise in the map to enhance the appearance of the detected clouds. The background noise is shown in Fig. A.1.

completely cover the CO(3–2) map, namely, SW bar, DarkPK, N66, and NE bar regions as shown in Fig. 1.

The SW bar and N66 CO(3–2) maps show high S/N values, so we determined $R_{32}$ using a pixel-by-pixel method. The first step in this procedure was to convolve the CO(3–2) data cubes to the CO(2–1) spatial resolution of 30″ by using a Gaussian beam of ∼22″. After convolution, both the CO(3–2) and CO(2–1) data cubes were resampled to a common spatial grid. Then, we integrated in velocity the data cubes using the moment masking method for both transitions (Dame 2011). Each data cube was smoothed to a beam two times the original spatial resolution beam and four times the channel width. This cube was masked to keep only those pixels where the intensity was above a threshold value of three times the S/N of the cubes. Finally, The resulting mask is used to integrate the original cube only within CO lines spectra that are considered as true brightness temperatures, avoiding spurious and unrealistic (e.g., spikes) emissions. These unrealistic emissions occur mainly in the SuperCAM data cubes that have pronounced non-uniform noise distributions (see Fig. A.1). A different mask was applied to each CO(3–2) and CO(2–1) cubes as these have different rms, which allows for the total CO distribution to be displayed for each transition. Finally, we calculated $R_{32}$ pixel-by-pixel using the integrated CO(3–2) and CO(2–1) maps masking those pixels that have $S/N \lesssim 3$ in intensity.

We used a different method to determine $R_{32}$ towards the DarkPK and NE bar, due to the non-uniform and much higher noise of the CO(3–2) cubes in these two regions. Instead of a pixel-by-pixel approach, we used the CO integrated spectrum towards the strongest clouds in the $J = 3$–2 transition identified in each region. We extracted the CO(3–2) and CO(2–1) integrated spectra from the convolved and regridded cubes at the peak of the cloud, that is, the pixel with maximum intensity in CO(3–2) at 30″ resolution (see Figs. 3 and 4). The velocity integrated emission ($I_{CO}$) in both transitions was calculated using

the zeroth-order moment method between the total width of the CO(2–1) lines and the $R_{32}$ was calculated as the ratio between both velocity integrated intensities.

## 4. Cloud identification

In addition to determining the $R_{32}$ ratio, we also identified the individual molecular clouds in CO(3–2) at 6 pc resolution. For the identification, we used the CPROPS algorithm (Rosolowsky & Leroy 2006) in the three SuperCAM CO(3–2) maps using the following criteria in the algorithm: clouds with sizes larger than the spatial resolution (20″), FWHM greater than three channels in velocity (>1.2 km s⁻¹) and 2 sigma above the noise level. So we fixed the CPROPS input parameters: MINAREA= 1 and MINCHAN= 3. The THRESHOLD input parameter (the cut in intensity to define "islands", see Rosolowsky & Leroy 2006) was fixed to 2. The EDGE input parameter was first set to 1.5 to 1.0 to extend the wing of the "islands". For EDGE = 1.5, only some tens clouds were identified with $S/N > 3$ in all three cubes. We changed to EDGE = 1, which extends the wing of the "islands" and we found many more but weaker clouds, some of which could be false CO emissions (e.g., spikes). To discriminate between these weaker true and false clouds, we extracted the spectrum of the cloud integrating on the area of the cloud as defined by its size and selected only those clouds that have an integrated spectral line with a velocity width larger than three adjacent channels (≃1.2 km s⁻¹) and temperatures ≳3× rms in the channels. We considered the clouds identified by these criteria as confirmed clouds.

The properties of the CO(3–2) clouds such as the radius ($R$ in pc), velocity dispersion ($\sigma_v$ in km s⁻¹), and CO flux ($F_{CO}$ in K km s⁻¹) given by CPROPS by mean of the moment method in the position-position-velocity data cube are summarized in Table 2. In Col. 1, we listed the identification (ID) number of
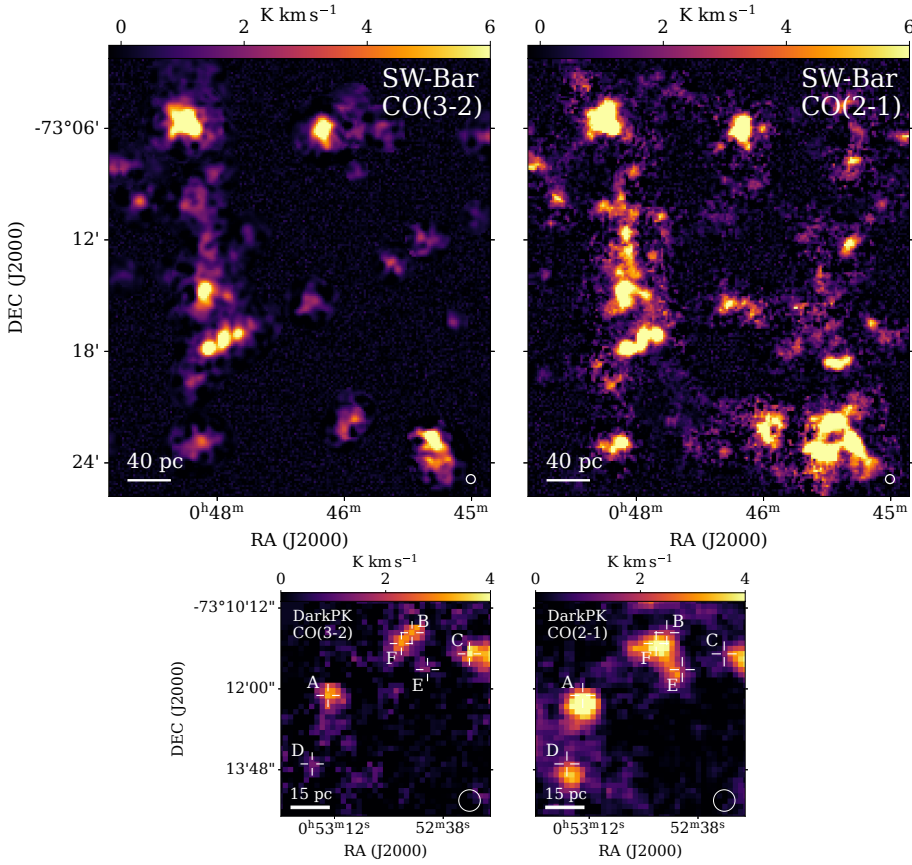
**Fig. 3.** Integrated CO emission in the SW bar and DarkPK. All maps were obtained with the moment-masked method. The left panels correspond to the transition $J = 3–2$, while the right panels show the CO emission in the transition $J = 2–1$. The spatial resolution of $30''$ is indicated in the bottom right corner of all maps. The upper panels show the SW bar CO(3–2) and CO(2–1) map used to determine the ratio represented by $R_{32}$ pixel-by-pixel. The lower panels show the DarkPK maps with white crosses indicating six positions (A, B, C, D, E, and F), where the CO(3–2) and CO(2–1) spectra were extracted to calculate $R_{32}$. A color-scaling bar is shown in the top of each map.
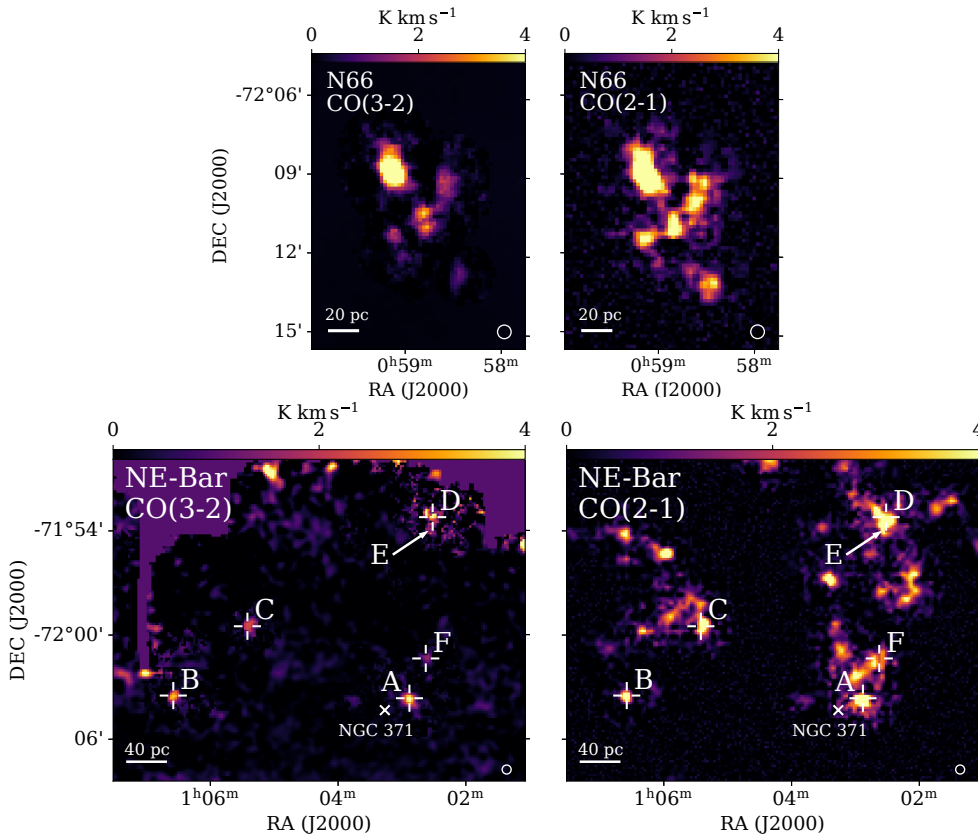


**Fig. 4.** Similar to Fig. 3, but for N66 and the NE bar. In the NE bar region, six CO sources (A–F) are indicated where $R_{32}$ was calculated.

**Table 2.** Physical parameters of CO(3–2) clouds in the SMC.

| ID | RA (hh:mm:ss.s) | Dec (dd:mm:ss) | $R$ (pc) | $V_{lsr}$ (km s$^{-1}$) | $\sigma_v$ (km s$^{-1}$) | $T_{peak}$ (K) | $I_{CO(3-2)}$ (caption) | $L_{CO(3-2)}$ (caption) | $M_{vir}$ ($10^3\,M_\odot$) |
|---|---|---|---|---|---|---|---|---|---|
| 14 | 00:46:27.38 | –73:29:49.6 | ... | 82.5 ± 1.3 | 1.1 ± 0.5 | 2.0 ± 0.4 | 0.4 ± 0.1 | 2.3 ± 0.5 | ... |
| 17 | 00:46:40.33 | –73:06:10.5 | 7.3 ± 1.1 | 126.0 ± 1.2 | 1.0 ± 0.1 | 2.5 ± 0.3 | 3.5 ± 0.4 | 19.1 ± 2.4 | 8.2 ± 2.6 |
| 28 | 00:47:43.51 | –73:17:06.5 | 4.5 ± 1.3 | 121.1 ± 1.8 | 1.6 ± 0.2 | 1.4 ± 0.2 | 1.9 ± 0.3 | 10.6 ± 1.5 | 11.5 ± 5.0 |
| 31 | 00:47:54.46 | –73:17:20.0 | 8.5 ± 0.8 | 120.8 ± 1.7 | 1.5 ± 0.2 | 1.7 ± 0.2 | 4.2 ± 0.3 | 23.2 ± 1.8 | 18.8 ± 5.1 |
| 39 | 00:48:05.71 | –73:17:51.1 | 5.6 ± 1.2 | 119.3 ± 2.3 | 2.0 ± 0.3 | 1.5 ± 0.2 | 2.9 ± 0.3 | 16.0 ± 1.7 | 22.7 ± 7.7 |
| 42 | 00:48:08.18 | –73:14:47.3 | 8.8 ± 1.0 | 120.5 ± 2.4 | 2.1 ± 0.3 | 1.5 ± 0.2 | 3.9 ± 0.4 | 21.3 ± 2.0 | 39.3 ± 11.9 |
| 56 | 00:48:17.75 | –73:05:17.2 | 3.8 ± 1.4 | 110.8 ± 1.1 | 0.9 ± 0.5 | 1.0 ± 0.2 | 0.4 ± 0.1 | 2.2 ± 0.7 | 3.4 ± 4.0 |
| 58 | 00:48:20.65 | –73:05:50.3 | 13.0 ± 0.8 | 113.6 ± 3.3 | 2.8 ± 0.2 | 1.6 ± 0.2 | 11.4 ± 0.5 | 62.8 ± 2.6 | 108.3 ± 18.0 |
| 59 | 00:48:22.06 | –73:10:13.8 | 5.2 ± 1.9 | 117.6 ± 1.2 | 1.0 ± 0.3 | 1.2 ± 0.2 | 0.9 ± 0.2 | 4.9 ± 0.9 | 5.2 ± 3.6 |
| 67 | 00:48:41.98 | –73:00:49.3 | 2.8 ± 1.6 | 126.9 ± 1.0 | 0.8 ± 0.4 | 2.1 ± 0.4 | 0.3 ± 0.1 | 1.7 ± 0.6 | 2.0 ± 2.1 |
| 69 | 00:48:56.39 | –73:09:54.1 | 3.1 ± 1.7 | 124.7 ± 1.0 | 0.8 ± 0.2 | 1.3 ± 0.2 | 0.6 ± 0.1 | 3.5 ± 0.6 | 2.2 ± 1.7 |
| 73 | 00:49:04.87 | –72:47:39.3 | 3.9 ± 1.4 | 133.6 ± 1.4 | 1.1 ± 0.5 | 2.1 ± 0.4 | 0.3 ± 0.1 | 1.5 ± 0.6 | 5.3 ± 5.3 |
| 85 | 00:49:44.72 | –73:24:27.3 | 4.2 ± 1.4 | 144.1 ± 1.1 | 1.0 ± 0.4 | 1.5 ± 0.3 | 0.8 ± 0.2 | 4.3 ± 1.1 | 4.0 ± 3.4 |
| 107 | 00:52:22.74 | –72:22:07.0 | ... | 194.5 ± 1.9 | 1.6 ± 0.5 | 5.5 ± 1.1 | 0.9 ± 0.1 | 4.7 ± 0.8 | ... |
| 145 | 00:58:35.61 | –72:27:31.1 | 3.7 ± 1.4 | 122.1 ± 1.7 | 1.4 ± 0.3 | 3.1 ± 0.5 | 1.1 ± 0.2 | 6.3 ± 1.0 | 7.9 ± 4.5 |
| 163 | 00:59:19.65 | –72:08:42.6 | 7.9 ± 1.2 | 159.3 ± 1.8 | 1.5 ± 0.2 | 3.2 ± 0.6 | 2.9 ± 0.4 | 16.0 ± 2.4 | 18.6 ± 5.8 |
| 165 | 00:59:21.01 | –72:08:54.4 | 6.6 ± 1.4 | 163.2 ± 1.6 | 1.4 ± 0.3 | 2.9 ± 0.6 | 1.5 ± 0.2 | 8.2 ± 1.3 | 12.7 ± 6.4 |
| 185 | 01:01:15.16 | –72:45:18.7 | 3.0 ± 1.6 | 162.6 ± 1.2 | 1.0 ± 0.3 | 6.1 ± 1.3 | 1.1 ± 0.2 | 6.0 ± 0.9 | 3.4 ± 2.7 |
| 195 | 01:01:46.64 | –72:14:34.1 | ... | 156.4 ± 0.9 | 0.7 ± 0.3 | 4.6 ± 0.9 | 0.5 ± 0.2 | 2.7 ± 1.0 | ... |
| 201 | 01:03:06.89 | –72:03:46.9 | 3.4 ± 1.8 | 168.9 ± 1.3 | 1.1 ± 0.5 | 3.8 ± 0.8 | 1.0 ± 0.3 | 5.4 ± 1.6 | 4.3 ± 4.2 |

**Notes.** $R$ is the deconvolved radius, $I_{CO(3-2)}$ and $L_{CO(3-2)}$ are in unit of $10^2$ K km s$^{-1}$ and $10^2$ K km s$^{-1}$ pc$^2$, respectively. This table only lists those clouds with $S/N \gtrsim 5$. A complete version of the table, with the 225 clouds identified with $S/N > 3$, can be found at the CDS. The ID numbers in Col. 1 follow the order of the complete table.

the clouds with high S/N ($\gtrsim$5). In Cols. 2 and 3, the right ascension and declination in J(2000) are indicated. In Cols. 4–10, we listed the radius ($R$), the local standard of rest velocity ($V_{lsr}$), the velocity dispersion ($\sigma_v$), the peak temperature ($T_{peak}$), the integrated CO(3–2) intensity ($I_{CO(3-2)}$), the CO(3–2) luminosity ($L_{CO(3-2)}$), and the virial mass ($M_{vir}$). The ID numbers in Table 2 refer to their number in the CDS table, which includes all clouds with $S/N > 3$. The CO cloud parameters are corrected by sensitivity bias and resolution bias, which is originated by the non-zero noise of CO emission and by the instrumental convolutions (finite spatial and spectral resolutions, see Rosolowsky & Leroy 2006). For the calculation of the radius, $R$, CPROPS uses the Solomon et al. (1987) definition for spherical clouds assuming a factor of 1.91 to convert the second moments of the emission along the major and minor axes of clouds ($\sigma_r$) to $R$. For unresolved clouds along the minor axis, we obtained the radii following Saldaño et al. (2023) calculation. The deconvolved $\sigma_v$ is calculated from Eq. (10) from Rosolowsky & Leroy (2006), and the FWHM of the spectral line is given by $\sqrt{8\ln(2)}\,\sigma_v$.

The CO flux of the clouds is converted to luminosity by mean:

$$L_{CO}[\text{K km s}^{-1}\text{ pc}^2] = F_{CO}(0\text{ K})[\text{K km s}^{-1}\text{ arcsec}^2](d[\text{pc}])^2$$
$$\times \left(\frac{\pi}{180 \times 3600}\right)^2, \quad (1)$$

where $F_{CO}(0\text{K})$ is the flux measured at infinite sensitivity, and $d$ is the distance of the galaxy in parsec of 60 kpc. Another important parameter used to analyze the stability of molecular clouds is the virial mass, given by the formula (Solomon et al. 1987):

$$M_{vir} = 1040\,\sigma_v^2\,R\ [M_\odot], \quad (2)$$

where $\sigma_v$ and $R$ are the corrected velocity dispersion and radius in parsec, respectively. For this last equation, a self-gravitating sphere with density profile $\rho \propto r^{-1}$ was assumed. The external forces, like magnetic fields and external pressure, are discarded.

The uncertainties in the properties and derived parameters are estimated by CPROPS with the bootstrapping technique. For the case of the unresolved clouds in which the sizes were recalculated, we estimated the error in the radius and virial mass calculation using the error propagation.

## 5. Results

### 5.1. CO(3–2) emission in the SMC bar

The distribution of the CO(3–2) emission in the SMC bar is shown in Fig. 2. The emission is found in many isolated clouds dispersed all over the SMC bar. Only two major strong emission concentrations are seen, one located in the SW bar and the other in the northern N66 region.

In Figs. 3 and 4, we show the CO(3–2) and CO(2–1) integrated emission maps for the SW bar, DarkPk, N66, and NE bar (see labels in Fig. 1). The integrated maps have the same spatial resolution of 30″. For the SW bar, the velocity range where the CO emissions were found is $100-150$ km s$^{-1}$, and for the DarkPk is between $130-165$ km s$^{-1}$. In the northern regions, N66 and NE bar, the velocity range of the CO emission is $140-170$ km s$^{-1}$ and $150-200$ km s$^{-1}$, respectively.

We found that most of the clouds in the SW bar and N66 regions are detected in both $J = 3-2$ and $J = 2-1$ transitions and only a few clouds show weak or even no CO(3–2) emission. For example, in N66, the plume-like component to the northeast and the bar structure to the southwest are well seen in the CO(3–2) as in the CO(2–1) map. In the case of the DarkPK, there are six positions where CO(3–2) and CO(2–1) emission is detected, labeled as A, B, C, D, E, and F in the bottom panels of Fig. 3.
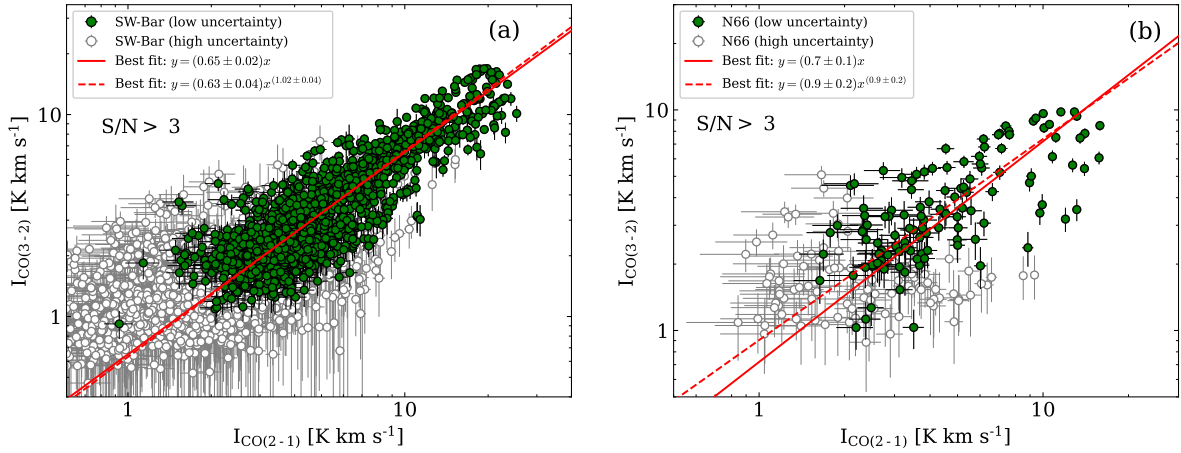
**Fig. 5.** Relationship between $I_{CO(3-2)}$ and $I_{CO(2-1)}$ for the SW bar and N66. The integrated emission in both transitions has $S/N > 3$. The green dots (indicated as low uncertainty) correspond to integrated emission with relative uncertainties <20% in both transitions. The white dots indicate integrated emissions with higher relative uncertainties. The solid and dashed red lines show the best fits of the low uncertainty data assuming a linear and a power-law model, respectively.

In the NE bar region, which has a CO(3–2) map with a higher noise level than the other observed regions of the SMC, we only detected reliable CO emission in six positions in the $J = 3-2$ transition, labeled as A, B, C, D, E, and F in the bottom panel of Fig. 4.

### 5.2. The CO(3–2)-to-CO(2–1) ratio in the SMC

We determined $R_{32}$ in the SMC using different methods depending on the region mapped. For the SW bar and N66 we used the pixel-by-pixel method to obtain the integrated emissions $I_{CO(3-2)}$ and $I_{CO(2-1)}$ as described in Sect. 3. In Fig. 5, we plot the correlation of both integrated emissions for the two regions. The correlation shows a linear trend in the log-log scale for the strong emission (low uncertainty), namely, that with lower than 20% uncertainties in both transitions and therefore not noise-dominated. Assuming that $I_{CO(3-2)}$ is proportional to $I_{CO(2-1)}$ and is represented by a linear model, $y = a\,x$, where the slope $a$ gives the integrated CO spectral line ratio ($R_{32}$), we find that the best fit for SW bar gives a slope of $a = 0.65 \pm 0.02$ (Fig. 5a) and a slightly higher slope of $a = 0.7 \pm 0.1$ for N66 (Fig. 5b). If we assume a power-law model ($y = \alpha\,x^{\beta}$), we find that the best fit has a power-law index of $\beta = 1.02 \pm 0.04$ and $\alpha = 0.63 \pm 0.04$ for SW bar and a power-law index of $\beta = 0.9 \pm 0.2$ and $\alpha = 0.9 \pm 0.2$ for N66. The uncertainties in our best fits were determined using the non-parametric (bootstrapping) technique in which we fit a number of subsets of data selected randomly from the original dataset to get a distribution for each free parameter (i.e., slope and $y$-intersection) and obtain their errors from the fifth percentiles. The scatter of the points in the $I_{CO(3-2)}$ and $I_{CO(2-1)}$ correlations for both regions increases for the weaker integrated emission, namely, for uncertainties higher than 20% (high uncertainty), an effect that could be atrributed to the lower S/N ratio of CO(3–2) compared to that of CO(2–1). The two model fits are shown in Fig. 5a for the SW bar and 5b for N66, respectively, and we adopted the linear fit slope result for the $R_{32}$.

As an alternative method to determine a median ratio of $R_{32}$ in the SW bar and N66, we made histograms from the $R_{32}$ maps (Fig. 6). These histograms are shown in Fig. 7 and were made with the pixel values of the $R_{32}$ maps with uncertainties lower than 30%. This limit was estimated to be consistent with the integrated CO emission of low uncertainty (<20%) in both transitions used in Fig. 5. We found that both histograms show

asymmetric shapes with median $R_{32}$ of $0.65^{+0.3}_{-0.2}$ and $0.8^{+0.4}_{-0.3}$. The estimated errors correspond to the 15th and 85th percentiles.

For the DarkPK and NE bar regions, we only estimated $R_{32}$ using the CO spectra obtained from the convolved and regridded CO(3–2) and CO(2–1) cubes at the peak positions of each identified cloud, as labeled in Figs. 3 and 4, respectively. In the DarkPK, we found $R_{32} \simeq 1-2$, with ~20–50% of uncertainty, in positions A, B, C, D, and E; this is higher than the median value 0.65 found in the SW bar, while in the F position, we found $R_{32} = 0.6 \pm 0.2$. On average, in the DarkPK region, the integrated CO line ratio is $R_{32} = 1.7 \pm 1.0$. In NE bar, we found a $R_{32} < 0.65$ in the clouds A and C, and $R_{32} > 0.65$ toward B, D, E, and F. On average, the integrated CO line ratio in the NE bar region is $R_{32} = 0.9 \pm 0.3$. All the CO spectra are shown in Fig. 8.

Since there could be a bias in the estimation of $R_{32}$ as we used different masks to constrain the CO spectral lines in both transitions to measure the integrated emission, as the CO(3–2) lines tend to be narrower than the CO(2–1) lines and the high noise of our CO(3–2) data cube may induce to an uncertain value of $I_{CO(3-2)}$, we checked this possibility by using a common mask in both transitions defined by the higher S/N of CO(2–1) in the SW bar and N66 regions. We did not find any significant differences in the data distribution of Fig. 5 used to fit the linear and power-law models. The selection of only the low-uncertainty (<20%) data set for the $R_{32}$ determination allowed us to measure high CO(3–2) integrated emission, which is not strongly affected by the spectral noise. In the case of DarkPK and NE bar, we used the full linewidth of CO(2–1) to measure the integrated emission in the CO(3–2) lines.

### 5.3. SMC CO(3–2) clouds

We have identified 225 CO clouds in the SMC with $S/N > 3$. Out of this total sample, 201 are well resolved clouds with non-deconvolved radii ≥3 pc corresponding to a deconvolved radii $R \geq 1.5$ pc. Increasing the $S/N \gtrsim$ to 5, we found 20 clouds, out of which 17 have resolved sizes. These 17 clouds are the brightest, well resolved CO clouds in the $J = 3-2$ transitions that we found in the SMC at 6 pc resolution. The parameters of these clouds are listed in Table 2[3].

---

[3] The complete table that includes the parameters of the 225 clouds can be found in the version available at the CDS.
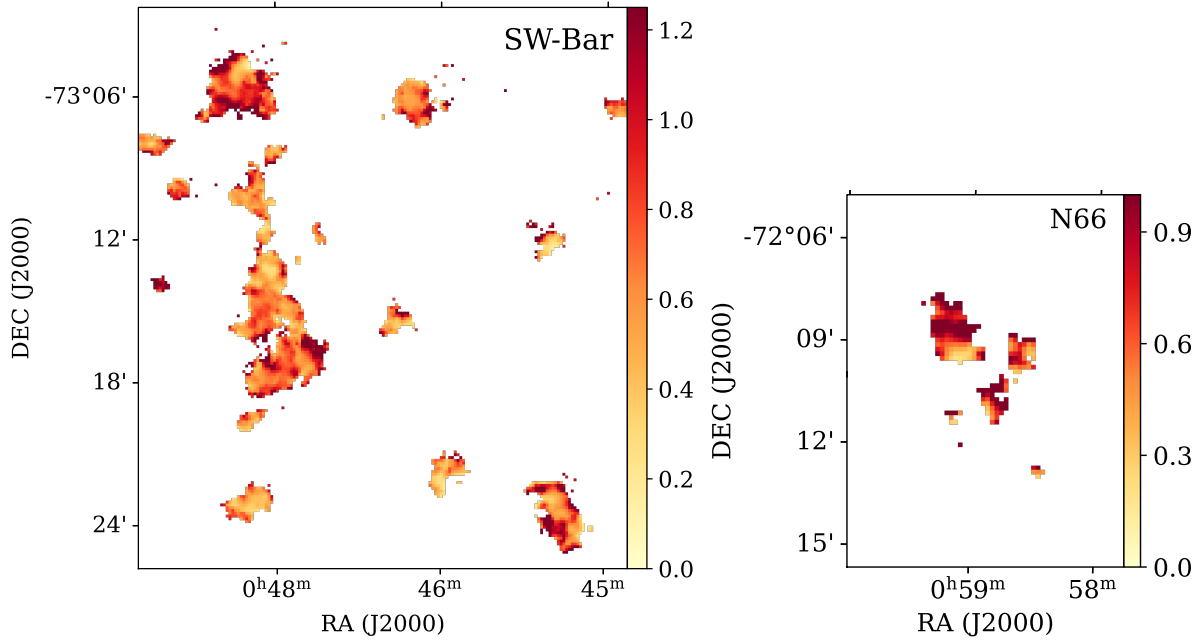
**Fig. 6.** $R_{32}$ maps of the SW bar and N66 regions at 30″ resolution. The $R_{32}$ scale is shown on the right of each map. This ratio maps correspond to $S/N > 3$ in integrated intensity in both transitions.
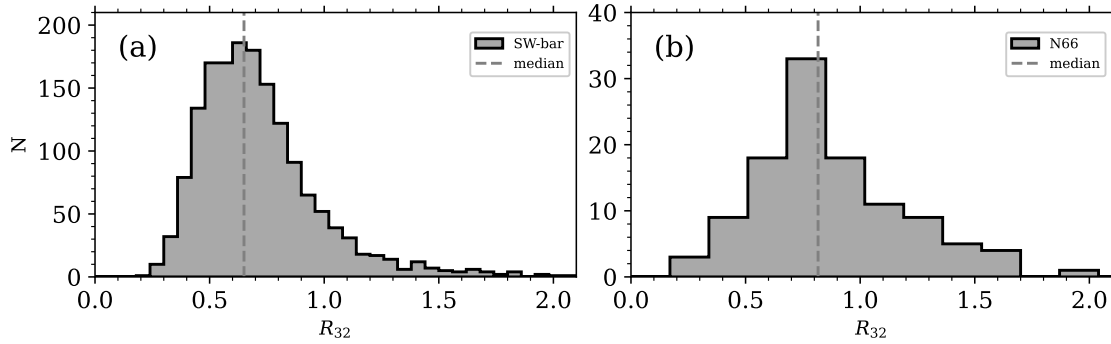


**Fig. 7.** Histograms of the pixel-by-pixel $R_{32} = [CO(3–2)/CO(2–1)]$ ratio for the SW bar and N66. The vertical dashed lines indicate the median $R_{32}$ of $0.65^{+0.30}_{-0.20}$ and $0.8^{+0.4}_{-0.3}$ for SW bar and N66, respectively.

We used all the CO(3–2) clouds identified by CPROPS to determine the scaling relations between their properties, namely, the linewidth-size, luminosity-size, luminosity-velocity dispersion, and virial mass-luminosity. In Fig. 9, we plotted the scaling relations for the CO(3–2) clouds with $S/N \gtrsim 5$ in black dots and the CO(3–2) clouds with S/N between 3 and 5 in white dots. However, we only performed linear fits in the log-log scales to these scaling relations using the brightest, well resolved clouds ($S/N \gtrsim 5$), as the parameters of clouds with low S/N values tend to be more uncertain (Rosolowsky & Leroy 2006) and will highly affect the linear fit in the scaling relation (see Wong et al. 2011). We followed the procedure indicated in Saldaño et al. (2023) and found the following relationships:

$$\log \sigma_v = (-0.38 \pm 0.09) + (0.7^{+0.1}_{-0.1}) \log R, \qquad (3)$$

$$\log L_{CO} = (1.1 \pm 0.3) + (2.5^{+0.3}_{-0.4}) \log R, \qquad (4)$$

$$\log L_{CO} = (2.5 \pm 0.1) + (3.7^{+1.0}_{-0.8}) \log \sigma_v, \qquad (5)$$

$$\log M_{vir} = (0.9 \pm 0.5) + (1.0^{+0.1}_{-0.2}) \log L_{CO}. \qquad (6)$$

The errors of these fits were estimated in a similar way to those fits shown in Sect. 5.2.

In each of the five panels of Fig. 9, we included the best fit obtained. For comparison, we plotted in blue the distribution of the CO(2–1) clouds which contains more than 90% of the CO(2–1) clouds with $S/N > 5$ (Saldaño et al. 2023). This dot density map is plotted in steps of 0.8, 0.4, 0.5, and 0.3 dex per unit area in panels a–d, respectively. In the panels, we include the inner Milky Way relationship (Solomon et al 1986).

The size-to-linewidth relation shows that the CO(3–2) clouds are below the Milky Way clouds (solid black line) of similar sizes by a factor of $1.3 \pm 0.3$. The comparison of the luminosity scaling relations between the SMC CO(3–2) and the Milky Way shows that the SMC clouds are under-luminous for similar sizes by a factor of $1.9 \pm 1.0$ and over-luminous for similar velocity dispersion by a factor of $1.7 \pm 1.6$, consistent with the Bolatto et al. (2008)'s results in the SMC but for coarser resolutions. The luminosity–virial mass relation (panel d) shows that for luminosities larger than $L_{CO} \sim 3$–$4 \times 10^3$, the CO(3–2) tend to have larger virial masses than their Milky-Way counterparts at a similar luminosity, while for clouds that are less luminous, the virial masses show a larger dispersion in their value. Thus, the scaling relations of the CO(3–2) are similar (within the error)
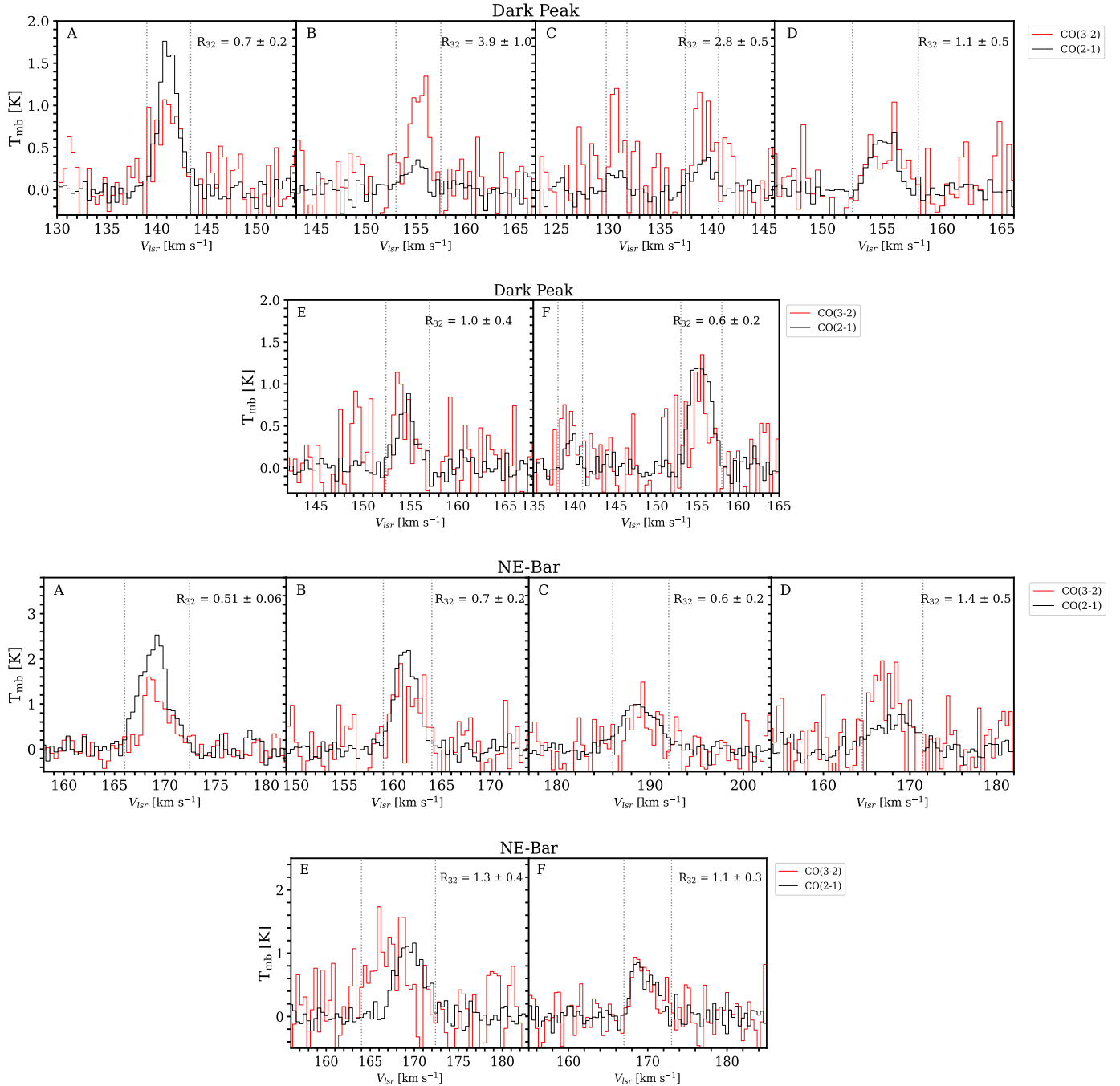
**Fig. 8.** CO(3–2) and CO(2–1) spectral lines toward DarkPK and NE bar. The CO(3–2) spectra are shown in red and the CO(2–1) spectra are in black. The CO spectral lines were extracted at the positions A, B, C, D, E, and F in the DarkPK and NE bar shown by crosses in Figs. 3 and 4, respectively. The integrated CO emission in both transitions was determined using the zeroth-moment within the velocity range shown in the vertical dotted lines. The derived ratio, $R_{32}$, is shown in the right upper corner of each panel.

to the CO(2–1) clouds scaling relations found by Saldaño et al. (2023).

Assuming virial conditions for the CO(3–2) clouds, we can estimate the CO-to-$H_2$ conversion factor ($\alpha_{CO(3-2)}$) as the ratio between the virial mass and CO luminosity. In panel e of Fig. 9, we plot the conversion factor as a function of the luminosity. We did not find an evident correlation between the CO luminosity and $\alpha_{CO(3-2)}$ (Spearman's $\rho = -0.02$). The distribution of the conversion factor of the CO(3–2) bright clouds has a median value of $11.7^{+5}_{-4}$ $M_\odot$ (K km s$^{-1}$ pc$^2$)$^{-1}$. Including those clouds with S/N between 3 and 5, then the median conversion factor is $12.6^{+10}_{-7}$ $M_\odot$ (K km s$^{-1}$ pc$^2$)$^{-1}$.

# 6. Discussion

## 6.1. The $R_{32}$ in the SMC

We found that the integrated CO line ratio, $R_{32}$, in the SMC ranges between $\sim$0.4 and $\sim$1.2, with some exceptions (discussed in this section). This range of values are consistent with $R_{32} \simeq 0.6$–0.8 found in low-metallicity galaxies with metallicities between 0.1–0.5 $Z_\odot$ (Hunt et al. 2017) and somewhat higher than the ratio ($R_{32} = 0.23$–0.59) found in the local group of low-mass dwarf galaxies (Leroy et al. 2022).

We found variations of the $R_{32}$ values which depend on the local environment of the observed region in the SMC. For
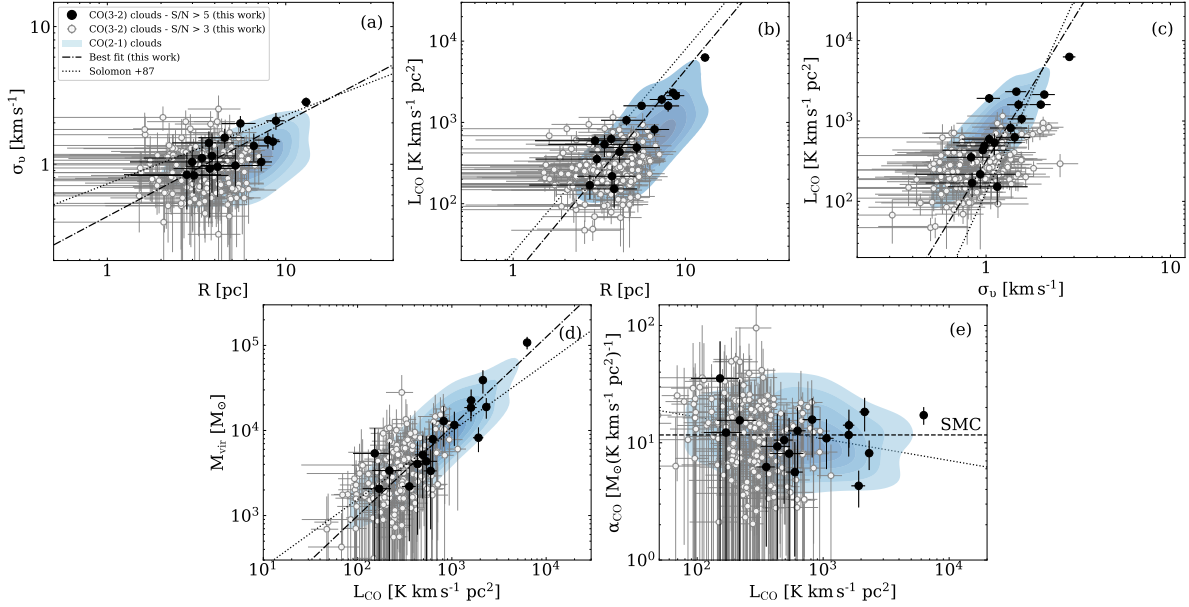
**Fig. 9.** Scaling relations of the CO(3–2) clouds parameters in the SMC. Panel a: size and linewidth relation ($\sigma_\nu - R$). Panel b: luminosity–size relation ($R - L_{CO}$). Panel c: Luminosity and linewidth relation ($\sigma_\nu - L_{CO}$). Panel d: Luminosity-virial mass relation ($L_{CO} - M_{vir}$). Panel e: CO-to-H$_2$ conversion factor-luminosity relation ($\alpha_{CO} - L_{CO}$). Black dots correspond to clouds with $S/N \gtrsim 5$, while the gray dots correspond to clouds with S/N between 3 and 5. For comparison, we plot the distribution of the CO(2–1) clouds in a blue color palette scale showing the concentration of the CO(2–1) clouds (Saldaño et al. 2023). In all the panels, the best fit for the brightest CO(3–2) clouds are indicated by dot-dashed lines. The Solomon et al. (1987) relation is indicated by dotted lines. Panel e: Dashed horizontal line indicates the median $\alpha_{CO(3-2)}$ of $12.6^{+20}_{-7}$ $M_\odot$ (K km s$^{-1}$ pc$^2$)$^{-1}$.

example, we estimated a median value of 0.65 in the SW bar, which is similar to the value in the quiescent SMCB1#1 cloud located in the southwest part of the SMC measured by Bolatto et al. (2005), although observed at a coarser 109″ (32 pc) resolution than ours at 30″ (9 pc). However, we found that more evolved and active star formation regions in the SW bar (N22, SWbarN, and SWbarS, associated to multiple HII regions; see Jameson et al. 2018) have a median ratio of $R_{32} = 0.7$–0.9, higher than the quiescent cloud (see Fig. B.1). This is also the case for N66, the brightest HII region of the SMC, which shows a $R_{32}$ of 0.7.

Inspecting the distribution of the $R_{32}$ values in the clouds, we found a high dispersion of $R_{32}$ in SW bar and N66, between 0.2 and 2.0 (see Fig. 7), which may be an indication of a dependence of $R_{32}$ on environmental local conditions (see Peñaloza et al. 2018). Figures B.1 and B.2 show that the highest values of $R_{32}$ are associated with strong emission at 8 μm and Hα, while lower values than 0.65 are found in regions that are either in the line-of-sight of the weakest HII regions or not associated to any HII region. Peñaloza et al. (2018) modeled the ISM evolution affected by the ISRF and found changes in the CO line ratios depending on the environmental conditions. They showed that $R_{32}$ can increase by a factor up to ~1.5–2.0 as the ISRF increases two orders of magnitudes, which would be consistent with our findings.

In the DarkPK, no association between CO(3–2) and 8 μm nor with Hα emission is seen. We found a result of $R_{32} > 1$ in clouds B, C, D, and E, (see Figs. 8 and B.1), while we found $R_{32} = 0.6$–0.7 in clouds A and F. These latter clouds are located in the border of two strong 8 μm sources. Such high ratios were not expected in this region as it has no signs of active star formation, it is dominated by ISRF, and has a low range of visual extinction with $A_V < 1$ (Jameson et al. 2018). In the DarkPK, the far-ultraviolet photons from evolved stellar sources controlling the gas heating and chemistry would dissociate more rapidly the CO(2–1) in the external part of the H$_2$ envelopes

than the CO(3–2) located in the innermost part of the molecular cloud. In this scenario, there could be a CO(2–1) deficiency that would increase $R_{32}$ above the median value found in the SW bar.

In the NE bar region, the integrated CO spectral line ratio towards cloud A is $R_{32} = 0.51 \pm 0.06$, while toward cloud B, C, D, E, and F, $R_{32} \geq 0.6$. Cloud A is on the low $R_{32}$ range found and it is not associated with strong 8 μm emission nor with HII regions, while clouds B, C, and D, are on the high $R_{32}$ range and are associated to the strongest peak emission at 8 μm and Hα (see Fig. B.2). Finally, clouds E and F, do not show any association with 8 μm and Hα, but have $R_{32} > 1$. These two clouds might be sharing similar features to the DarkPK clouds with high $R_{32}$.

### 6.2. Environment dependence of $R_{32}$ in the SMC

To explore the dependence of $R_{32}$ with observational properties, we made correlations with CO emission, FIR color, and total IR (TIR) surface brightness which trace star formation activity. We used the intensity of CO(2–1) and CO(3–2) shown in our study, the Herschel bands (100–250 μm) from HERITAGE (Gordon et al. 2014), and the Spitzer MIPS 24, 70 and 160 μm from SMC-SAGE (Gordon et al. 2011). The HERITAGE maps at 40″ resolution are regridded to a 56″ pixel size, so we convolved and regridded all our images to have common resolution and spatial grid maps. In this analysis, the parameters estimated by the integrated maps of both SW-bar and N66 CO data cubes were used jointly and are referred to as SMC bar in the plots.

We show in Fig. 10a, b, the correlation of $R_{32}$ with the integrated intensity $I_{CO(3-2)}$ and $I_{CO(2-1)}$, respectively. We found a very weak correlation of $R_{32}$ with $I_{CO(3-2)}$ with a Spearman's correlation $\rho_S = 0.4$. At high brightness temperature in the CO $J = 3$–2 transition, reliable values of $R_{32}$ (lower uncertainty than ~25%) tend to have values higher than the median
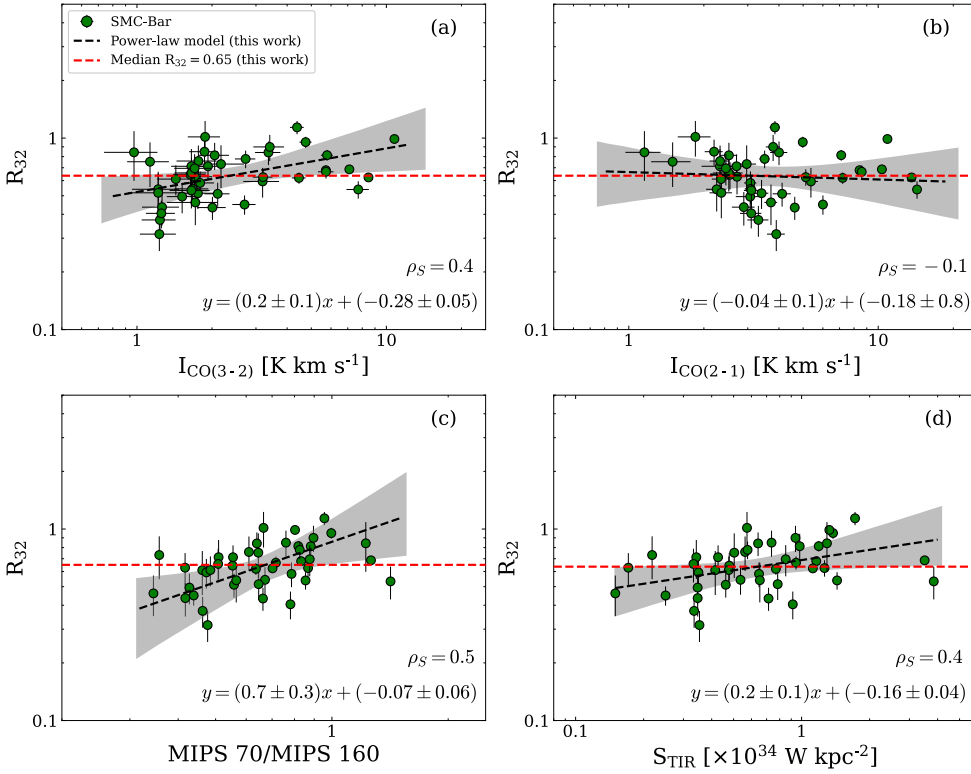
**Fig. 10.** Environment dependence of $R_{32}$. The ratio (with uncertainty lower than ~25%) is correlated with the local intensity of CO(3–2) and CO(2–1) in panels (a) and (b), respectively. In panel (c), $R_{32}$ as a function of the far-infrared (FIR)color of the Spitzer MIPS bands (Gordon et al. 2011), and in panel (d), $R_{32}$ as a function of the TIR surface brightness from Spitzer and Herschel bands (Gordon et al. 2011, 2014). The red and black dashed lines in all panels indicate the median value of $R_{23}$ and the best fit, respectively. The Spearman's correlations ($\rho_S$) and the best-fit equations (in log–log scale) are located in the right bottom corners.

value 0.65 determined for the SMC bar. However, in low-brightness-temperature regions, $R_{32}$ shows a higher dispersion with values lower than the median. On the contrary, $R_{32}$ do not show a correlation with $I_{CO(2-1)}$ (Spearman's correlation is $\rho_S = -0.1$).

The correlation of $R_{32}$ with the FIR color [70/160] of the Spitzer bands is shown in panel c of Fig. 10. The $R_{32}$ increases for higher values of the FIR color and the best fit has a Spearman's coefficient of $\rho_S = 0.5$. For environments with FIR colors [70/160] larger than 0.8, most of the $R_{32}$ values are above the median of 0.65 determined for the SMC bar. This result on the FIR color-line ratio correlation is similar to findings in nearby disk galaxies (den Brok et al. 2021), although these studies use the integrated spectral line CO(2–1)-to-CO(1–0) ratio ($R_{21}$) instead of $R_{32}$. As the FIR color trace dust temperatures and also ISRFs, $R_{32}$ in the SMC bar is found higher in active star-forming regions, where the ISRF, dust temperature, and the density of the gas are expected to be higher.

Finally, we correlated $R_{32}$ with the TIR surface brightness in the SMC bar, as shown in panel d of Fig. 10. We determined the TIR surface brightness following the same method described in Jameson et al. (2018). The Spitzer MIPS 24 and 70 μm bands are combined to the Herschel 100, 160, and 250 μm bands by using the equation $S_{TIR} = \sum c_i S_i$. Here, $S_{TIR}$ is the TIR surface brightness, and $S_i$ is the brightness in the given Spitzer and Herschel bands, $i$. Both are in the unit of W kpc$^{-2}$ and $c_i$ is the calibration coefficient from combined brightness provided by Galametz et al. (2013). We found a moderate correlation between $R_{32}$ and the TIR surface brightness (Spearman's coefficient of $\rho_S \simeq 0.4$). $R_{32}$ tends to be lower than the median value for low-TIR surface brightness, while $R_{32}$ tends to increase above the median value for higher TIR surface brightness. The TIR surface brightness scales with the molecular gas surface density, where we expect that the star formation activity may be embedded. Our finding indicates that $R_{32}$ in the SMC bar tends to be higher in very active and dense star-forming regions.

These correlations could be useful to consider when using $R_{32}$ as a diagnostic for environmental properties in external galaxies. To improve these correlations, higher sensitivity observations are needed to allow for the ranges in the observed properties to be expanded. Moreover, the coarser resolution of the Spitzer and Herschel data used does not allow us to study the smaller structures resolved in this work since the ISM properties are averaged over larger areas.

Considering these caveats, our results indicate that in general, typical values of the ratio, $R_{32} \sim 0.7$–$1.0$, are found toward active star-forming regions. These regions are usually excited by HII regions and/or shock emission; whereas lower $R_{32}$ ratios ($\lesssim 0.6$) were found in more quiescent regions. This behavior is consistent with those found in other galaxies and in semi-analytic studies of the ISM in which $R_{32}$ (including ratios in other transitions) increase in more active star-forming regions and/or denser and hotter gas, poorly shielded by dust (Peñaloza et al. 2018; Celis Peña et al. 2019; den Brok et al. 2021; Leroy et al. 2022).

### 6.3. Scaling Relation in the SMC

We identified 225 CO clouds in the $J = 3$–$2$ transition at 6 pc resolution and we determined their main properties: $R$, $\sigma_v$, $L_{CO}$, and $M_{vir}$. However, we only used 17 high S/N ($\gtrsim 5$) clouds in analyzing the scaling relationships due to the limited sensitivity of our CO(3–2) survey. Despite the low number of clouds with high S/N, our results are consistent with the study of the scaling relations in the SMC obtained at different spatial resolutions, from 1 to 100 pc (Bolatto et al. 2008; Saldaño et al. 2018, 2023; Kalari et al. 2020; Ohno et al. 2023). It seems that independent of the $J$-transitions and the cloud identification algorithm used, the cloud properties in the scaling relationships would be intrinsic to the SMC.

The size-to-linewidth relationship (Fig. 9a) shows that the CO(3–2) clouds are below the Milky-Way clouds of similar size

by a factor of 1.3. In the CO(2–1) survey conducted on the SMC, this deviation is present at a factor of ∼2 (Saldaño et al. 2023); these authors suggested that it might be due to the small CO cloudlets in the SMC that cannot trace the total turbulence of larger $H_2$ envelopes (see Bolatto et al. 2008). They also discard a deficit of turbulent kinetic energy in CO clouds since these clouds would be gravitationally bounded to explain such departure in the size-to-linewidth relation. Ohno et al. (2023) showed similar results, finding a departure factor of 1.5 below the Milky-Way trend in their CO(2–1) survey at 2 pc resolution in the SMC. These authors ascribe this departure to lower column densities (by a factor of 2) than those in Milky Way clouds of similar size.

Finally, the $\alpha_{CO(3-2)}$ correlation with $L_{CO(3-2)}$, is shown in panel (e) of Fig. 9. The plot shows a flattened distribution of $\alpha_{CO(3-2)}$ values between $10^2$–$10^4$ K km s$^{-1}$ pc$^2$ for the brightest clouds (S/N ≳ 5) with a median value of $11.7^{+5}_{-4}$ $M_\odot$ (K km s$^{-1}$ pc$^2$)$^{-1}$ at 6 pc resolution. We also determined the median value using all the 225 CO(3–2) clouds with $S/N > 3$ identified and we found a quite similar value of $\alpha_{CO(3-2)}$ of $12.6^{+10}_{-7}$ $M_\odot$ (K km s$^{-1}$ pc$^2$)$^{-1}$. These $\alpha_{CO(3-2)}$ values are not very different to other SMC determinations. For example, Saldaño et al. (2023) found $\alpha_{CO(2-1)}$ of $10.5 \pm 5$ $M_\odot$ (K km s$^{-1}$ pc$^2$)$^{-1}$ using the CO(2–1) 9 pc resolution survey of the SMC using this same methodology. Moreover, convolving the CO(3–2) SW and N66 maps to 9 pc, we found that $\alpha_{CO(3-2)}$ is $14.5^{+8}_{-7}$ $M_\odot$ (K km s$^{-1}$ pc$^2$)$^{-1}$, a bit higher than that estimated at 6 pc. Despite the uncertainties in the determination of the conversion factors, $\alpha_{CO(3-2)}$ tend to be higher than $\alpha_{CO(2-1)}$ by a factor of ∼1.4, which agrees with our estimation of $1/R_{32} \sim 1.5$. This result is expected for CO clouds that tend to have lower luminosities at higher J-transitions, while the virial mass would not change considerably.

The determination of the properties of the clouds is sensitive to the cloud definitions which are biased by the S/N of the observations. Both $R$ and $L_{CO}$ have limitations as they are dependent on the true extension of the CO cloud and these are sensitive to the quality of the data. Therefore, the virial mass determination and the CO luminosity are sensitive to the size of the cloud. In our case, it is interesting to note that although the CO(3–2) data has less sensitivity but it has much better spatial resolution than the CO(2–1) data, we obtain $\alpha_{CO(3-2)}$ values which are similar to that derived at CO(2–1). The SMC, like other low metallicity environments, has a reduced size of the CO distribution within the total $H_2$ clouds with a significant fraction of CO-dark gas underestimating the CO-to-$H_2$ conversion factor. Using dust-based $\alpha_{CO}$ determination, Saldaño et al. (2023) found a higher conversion factor than the virial-based conversion factor by a factor of ∼3. Undoubtedly, higher sensitivity and higher resolution maps are needed to better determine the conversion factor.

## 7. Conclusions

The main conclusion of the SuperCAM CO(3–2) survey can be summarized as follows:

1. We determine value of $R_{32}$ in the SMC and found $R_{32} = 0.65 \pm 0.02$ for the SW bar and a slightly higher value of $R_{32} = 0.7 \pm 0.1$ in N66;

2. The $R_{32}$ values depend on the local environmental conditions of the region. For quiescent regions, $R_{32} \lesssim 0.6$ were found. In the case of active star-forming regions, $R_{32}$ is between ∼ 0.7–1.0;

3. We identified 225 CO(3–2) clouds at 6 pc resolution in the SMC bar. The total luminosity in the $J = 3–2$ transition is $(2.2 \pm 0.3) \times 10^4$ K km s$^{-1}$ pc$^2$ within the mapped region;

4. The CO(3–2) clouds follow similar scaling relations as the CO(2–1) clouds. We found that the size-to-linewidth relation, for the CO(3–2) clouds, is below the Milky Way clouds of similar size by a factor of 1.3;

5. Assuming that the CO(3−2) clouds are virialized, we determined a median $\alpha_{CO(3-2)} = 12.6^{+10}_{-7}$ $M_\odot$ (K km s$^{-1}$ pc$^2$)$^{-1}$ for the total sample at a 6 pc resolution.

## References

Bolatto, A. D., Leroy, A., Israel, F. P., & Jackson, J. M. 2003, ApJ, 595, 167
Bolatto, A. D., Israel, F. P., & Martin, C. L. 2005, ApJ, 633, 210
Bolatto, A. D., Leroy, A. K., Rosolowsky, E., Walter, F., & Blitz, L. 2008, ApJ, 686, 948
Bolatto, A. D., Wolfire, M., & Leroy, A. K. 2013, ARA&A, 51, 207
Celis Peña, M., Paron, S., Rubio, M., Herrera, C. N., & Ortega, M. E. 2019, A&A, 628, A96
Dame, T. M. 2011, arXiv e-prints [arXiv:1101.1499]
den Brok, J. S., Chatzigiannakis, D., Bigiel, F., et al. 2021, MNRAS, 504, 3221
Galametz, M., Kenicutt, R. C., Calzetti, D., et al. 2013, MNRAS, 431, 1956
Gordon, K. D., Meixner, M., Meade, M. R., et al. 2011, AJ, 142, 102
Gordon, K. D., Roman-Duval, J., Bot, C., et al. 2014, ApJ, 797, 85
Groppi, C., Walker, C., Kulesa, C., et al. 2010, in Twenty-First International Symposium on Space Terahertz Technology, 368
Güsten, R., Nyman, L. Å., Schilke, P., et al. 2006, A&A, 454, L13
Hilditch, R. W., Howarth, I. D., & Harries, T. J. 2005, MNRAS, 357, 304
Hunt, L. K., Weiß, A., Henkel, C., et al. 2017, A&A, 606, A99
Jameson, K. E., Bolatto, A. D., Wolfire, M., et al. 2018, ApJ, 853, 111
Kalari, V. M., Rubio, M., Saldaño, H. P., & Bolatto, A. D. 2020, MNRAS, 499, 2534
Kalberla, P. M. W., Kerp, J., & Haud, U. 2020, A&A, 639, A26
Kloosterman, J., Cottam, T., Swift, B., et al. 2012, SPIE Conf. Ser., 8452, 845204
Leroy, A. K., Rosolowsky, E., Usero, A., et al. 2022, ApJ, 927, 149
Minamidani, T., Mizuno, N., Mizuno, Y., et al. 2008, ApJS, 175, 485
Mizuno, N. 2009, in The Magellanic System: Stars, Gas, and Galaxies, 256, eds. J. T. Van Loon, & J. M. Oliveira, 203
Mizuno, N., Rubio, M., Mizuno, A., et al. 2001, PASJ, 53, L45
Mizuno, Y., Kawamura, A., Onishi, T., et al. 2010, PASJ, 62, 51
Muller, E., Mizuno, N., Minamidani, T., et al. 2014, PASJ, 66, 4
Nikolić, S., Garay, G., Rubio, M., & Johansson, L. E. B. 2007, A&A, 471, 561
Ohno, T., Tokuda, K., Konishi, A., et al. 2023, ApJ, 949, 63
Oliveira, J. M., van Loon, J. T., Sloan, G. C., et al. 2011, MNRAS, 411, L36
Oliveira, J. M., van Loon, J. T., Sewiło, M., et al. 2019, MNRAS, 490, 3909
Peñaloza, C. H., Clark, P. C., Glover, S. C. O., & Klessen, R. S. 2018, MNRAS, 475, 1508
Pineda, J. L., Langer, W. D., Goldsmith, P. F., et al. 2017, ApJ, 839, 107
Requena-Torres, M. A., Israel, F. P., Okada, Y., et al. 2016, A&A, 589, A28
Roman-Duval, J., Bot, C., Chastenet, J., & Gordon, K. 2017, ApJ, 841, 72
Rosolowsky, E., & Leroy, A. 2006, PASP, 118, 590
Rubio, M., Contursi, A., Lequeux, J., et al. 2000, A&A, 359, 1139
Russell, S. C., & Dopita, M. A. 1992, ApJ, 384, 508
Saldaño, H. P., Rubio, M., Jameson, K., & Bolatto, A. D. 2018, Bol. Asoc. Argentina Astron. Plata Argentina, 60, 192
Saldaño, H. P., Rubio, M., Bolatto, A. D., et al. 2023, A&A, 672, A153
Seifried, D., Haid, S., Walch, S., Borchert, E. M. A., & Bisbas, T. G. 2020, MNRAS, 492, 1465
Solomon, P. M., Rivolo, A. R., Barrett, J., & Yahil, A. 1987, ApJ, 319, 730
Stanke, T., Arce, H. G., Bally, J., et al. 2022, A&A, 658, A178
Walker, C., Groppi, C., Kulesa, C., et al. 2005, in Sixteenth International Symposium on Space Terahertz Technology, 427
Winkler, P. F., Smith, R. C., Points, S. D., & MCELS Team. 2015, in ASP Conf. Ser., 491, Fifty Years of Wide Field Studies in the Southern Hemisphere: Resolved Stellar Populations of the Galactic Bulge and Magellanic Clouds, eds. S. Points, & A. Kunder, 343
Wolfire, M. G., Hollenbach, D., & McKee, C. F. 2010, ApJ, 716, 1191
Wong, T., Hughes, A., Ott, J., et al. 2011, ApJS, 197, 16
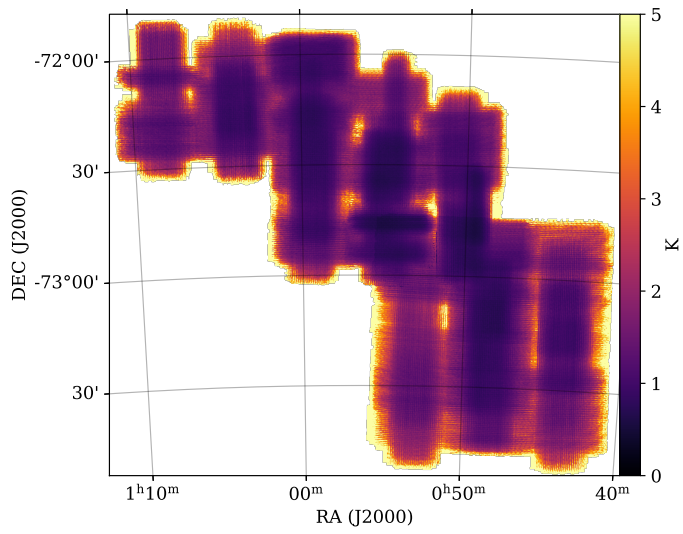
## Appendix A: RMS total map



**Fig. A.1.** RMS map of the SuperCAM observation toward the SMC bar. The RMS median value ~1.0 K *rms* with a range between 0.1 and 5 K (color bar). Values do not consider the borders of the rms map.

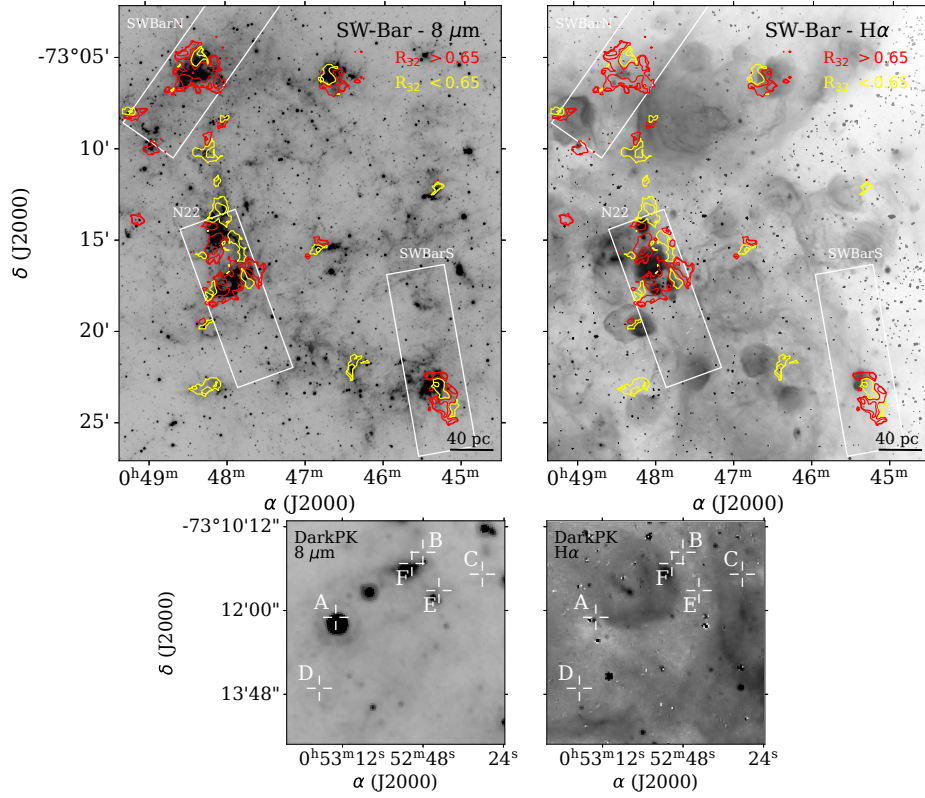## Appendix B: $R_{32}$ distribution in star-forming regions



**Fig. B.1.** Spatial distribution of $R_{32}$ (colored contours) overlapping on the Spitzer 8 μm (left panels) and Hα emission (right panels) in grayscale for the SW-BAR and DarkPK regions. The yellow and red contours on the top panels correspond to $R_{32} = 0.2,\ 0.4,\ 0.6$ and $0.7,\ 1.0,\ 2.0$, respectively. In the bottom panels, the crosses A, B, C, D, E, and F, indicate the position where $R_{32}$ was estimated (see Fig. 8).
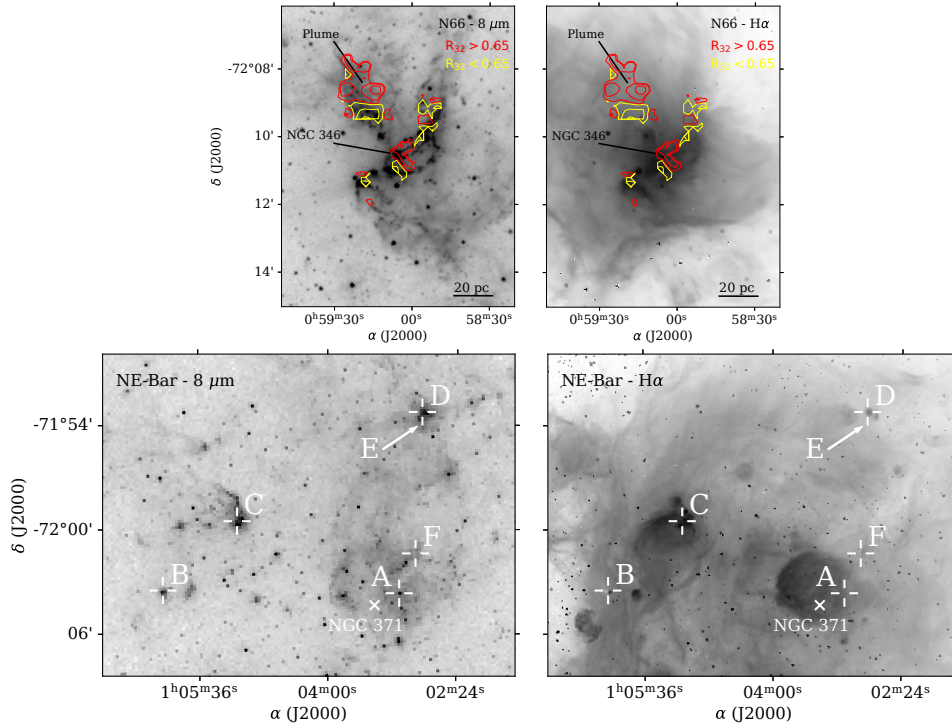


**Fig. B.2.** Similar to Fig. B.1 but for N66 and NE bar.